Mon. Not. R. Astron. Soc. **364,** 607–619 (2005) doi:10.1111/j.1365-2966.2005.09579.x

Morphological evolution of discs in clusters

Chiara Mastropietro,[1⋆] Ben Moore,[1] Lucio Mayer,[1] Victor P. Debattista,[2,3] Rocco Piffaretti[1,4] and Joachim Stadel[1]

[1]*Institute for Theoretical Physics, University of Zürich, CH-8057 Zürich, Switzerland*
[2]*Astronomy Department, University of Washington, Seattle, WA 98195-1580, USA*
[3]*Institut für Astronomie, ETH Zürich, CH-8093 Zürich, Switzerland*
[4]*Institut für Astrophysik, Leopold-Franzens Universität Innsbruck, A-6020 Innsbruck, Austria*

Accepted 2005 September 1. Received 2005 September 1; in original form 2004 November 19

ABSTRACT

The recent discovery of hidden non-axisymmetric and disc-like structures in bright Virgo dwarf elliptical and lenticular galaxies (dE/dSph/dS0) indicates that they may have late-type progenitors. Using *N*-body simulations we follow the evolution of disc galaxies within a Λ cold dark matter (ΛCDM) cluster simulated with 10^7 particles, where the hierarchical growth and galaxy harassment are modelled self-consistently. Most of the galaxies undergo significant morphological transformation, even at the outskirts of the cluster, and move through the Hubble sequence from late-type discs to dwarf spheroidals. None of the discs is completely destroyed, therefore they cannot be the progenitors of ultracompact dwarf (UCD) galaxies. The time evolution of the simulated galaxies is compared with unsharp masked images obtained from Very Large Telescope (VLT) data and the projected kinematics of our models with the latest high-resolution spectroscopic studies from the Keck and Palomar telescopes.

Key words: methods: *N*-body simulations – galaxies: clusters: general – galaxies: dwarf – galaxies: evolution.

1 INTRODUCTION

Early-type dwarfs (dE and dSO) are the most common type of galaxies in the nearby universe, yet their origin is still unknown. These galaxies are found nearly exclusively near bright galaxies and in groups or clusters. Their continuation or separation from the brighter elliptical sequence is currently debated (Graham & Guzmán 2003; Gavazzi et al. 2005). Formation scenarios include mainly two different hypotheses: (i) dEs and dSOs are primordial galaxies, (ii) they are the result of a morphological transformation of spiral and irregular galaxies accreting into the cluster. This latter idea is supported by some observations, i.e. the relative number density of dwarf early-type galaxies increases with the local galaxy density (Ferguson & Sandage 1991), suggesting that the environment drives galaxy evolution. Kormendy & Freeman (2004) investigated the systematic properties of dark matter haloes in late-type and dwarf spheroidal galaxies concluding that they form a single physical sequence as a function of the dark matter core mass. Moore, Lake & Katz (1998) have shown that galaxy harassment in clusters can transform spirals into spheroidals. Harassment can explain the morphological evolution of the small spiral and irregular galaxies observed in clusters at redshift $z \sim 0.4$ (Dressler et al. 1994) into dwarf ellipticals in the nearby universe (Moore et al. 1996). Moreover, the radial velocities of early-type galaxies in the Virgo cluster seem to indicate that these galaxies are not an old cluster population (Conselice, Gallagher & Wyse 2001), but originate from infalling field galaxies. According to this evolutionary scenario, we expect to find nearby cluster galaxies that are currently undergoing morphological transformation and retain part of their disc nature. Recent observations confirm that early-type galaxies have a broad range of photometric and kinematical characteristics. Jerjen, Kalnajs & Binggeli (2000) and Barazza, Binggeli & Jerjen (2002) discovered hidden spiral structures and bar features in five bright dEs in the Virgo cluster, concluding that a sizeable fraction of all bright early-type dwarfs hosts a disc component. Spirals and discs were also observed within dwarf spheroidal galaxies in the Coma (Graham & Guzmán 2003) and Fornax clusters (De Rijcke et al. 2001). Furthermore, the degree of rotational support is found to vary from 0 to a value close to 1 expected for a galaxy flattened by rotation (De Rijcke et al. 2001; Pedraz et al. 2002; Simien & Prugniel 2002; Geha, Guhathakurta & van der Marel 2003; van Zee, Skillman & Haynes 2004a). The aim of this work is to follow the evolution of disc galaxies orbiting in a cluster environment using high-resolution *N*-body simulations and to compare the final harassed remnants with the latest photometric and spectroscopic data. Previous studies have suffered from low resolution, and they used idealized cluster models for the initial conditions. We aim to use sufficient resolution that we can follow the detailed morphological evolution, and we evolve the galaxy models within a cluster selected from a cosmological simulation. In addition, the model has cuspy cold dark matter (CDM) haloes and structural

⋆E-mail: chiara@physik.unizh.ch

parameters as expected in the concordance cosmological model. This study complements that of Gnedin (2003), who studied the evolution of luminous early-type disc galaxies within a cosmological context.

The paper is organized as follows. In Section 2, we present the main characteristics of the galaxy models and the ΛCDM cluster used. The results of the three-dimensional simulations are illustrated in Section 3, while in Sections 4 and 5, we report a projected photometric and kinematical analysis of the simulated remnants and the comparison with observations.

2 SIMULATIONS

All the simulations have been carried out using PKDGRAV, a parallel multistepping N-body tree code designed for high-force accuracy (Stadel 2001).

The galaxy model is a multicomponent system with a stellar disc embedded in a spherical dark matter halo and was constructed using the technique described by Hernquist (1993). The dark matter distribution initially follows a NFW (Navarro, Frenk & White 1996, 1997) profile, which is adiabatically contracted in response to baryonic infall (Springel & White 1999). The disc has an exponential surface density profile of the form

$$\Sigma(R) = \frac{M_{\rm d}}{2\pi {R_{\rm d}}^2} \exp\left(-R/R_{\rm d}\right), \quad (1)$$

where $M_{\rm d}$ and $R_{\rm d}$ are, respectively, the disc mass and radial scalelength (in cylindrical coordinates), while the thin vertical structure is characterized by the scaleheight $z_{\rm d}$, which sets the 'temperature' of the disc

$$\rho_{\rm d}(R, z) = \frac{\Sigma(R)}{2z_{\rm d}} \,{\rm sech}^2\left(z/z_{\rm d}\right). \quad (2)$$

The structural parameters of the disc and the halo are chosen so that the resulting rotation curve resembles that of a typical bulgeless late-type (Sc/Sd) disc galaxy (Courteau 1997; Persic & Salucci 1997). The model parameters are initialized following the same procedure as Mayer et al. (2002), which was based on the galaxy formation model of Mo, Mao & White (1998). The mass within the virial radius was set equal to 7×10^{10} $\rm M_\odot$ and the fraction of mass in the disc is ∼6 per cent. The contribution of the different components to the global rotation curve, assuming a disc scalelength $R_{\rm d} =$ 1.5 kpc and a concentration $c = 10$ (where c is defined as $c = r_{\rm vir}/r_{\rm s}$, with $r_{\rm vir}$ and $r_{\rm s}$, respectively, virial and scale radius of the NFW halo) is plotted in Fig. 1. The halo spin parameter, which sets the disc scalelength in our modelling, is $\lambda = 0.045$, where λ relates the angular momentum, J, and the total energy, E, of a system with virial mass $M_{\rm vir}$ through the relation $\lambda = J|E|^{1/2}G^{-1}M_{\rm vir}^{-5/2}$. The model has a central surface brightness $\mu_{\rm B} = 22$ mag arcsec^{-2}, assuming an initial V-band mass-to-light ratio $(M/L) \simeq 4$ (Geha, Guhathakurta & van der Marel 2002) and a $B - V$ colour of 0.77 (van Zee, Barton & Skillman 2004b). The stellar disc satisfies the Toomre (Toomre 1964) stability criterion, which requires, for a rotational supported disc

$$Q_{\rm star}(R) = \frac{\sigma_{\rm R} k}{3.36 G \Sigma_{\rm s}} > 1, \quad (3)$$

where $\sigma_{\rm R}$ is the radial velocity dispersion, κ is the local epicyclic frequency and $\Sigma_{\rm s}$ the stellar surface density. The efficiency of swing amplification of a disc perturbation with m-fold symmetry is governed by a combination of Q and the parameter $X_m = \kappa^2 R/(4\pi m G \Sigma_{\rm s})$ (Toomre 1981). The radial profiles of Q and X_2 are indicated in Fig. 2.

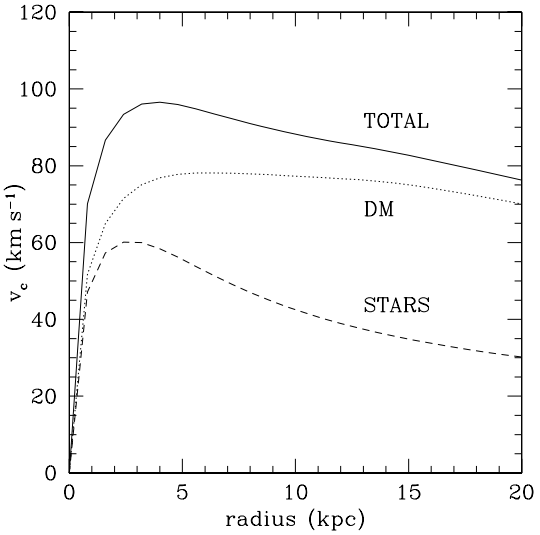

Figure 1. The rotation curve of the initial galaxy model. The stellar and dark matter contributions to the total rotation curve are indicated.

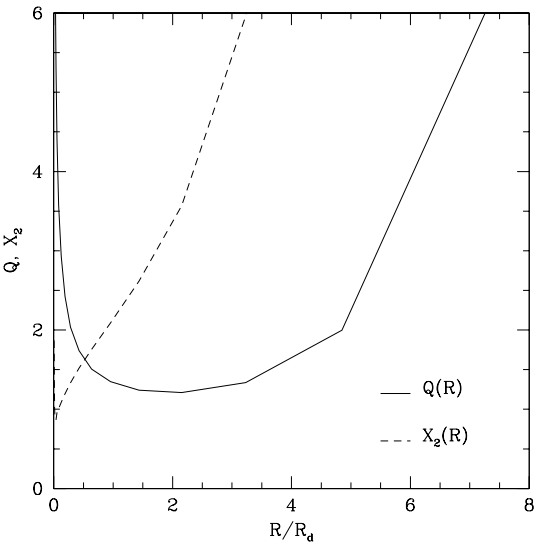

Figure 2. Q and X_2 parameters as function of radius (in units of the disc scalelength, $R_{\rm d}$).

Each galaxy is modelled with 10^6 particles, 10^5 of which are in the disc. The gravitational softening is set to 0.5 kpc for the dark halo and 0.1 kpc for the disc particles. The galaxies were evolved for ∼5 Gyr in a ΛCDM cluster with a mass at $z = 0$ comparable to that of Virgo ($M_{\rm vir} = 3.1 \times 10^{14}$ $\rm M_\odot$), concentration $c_{\rm NFW} = 8.8$ and a virial radius $R_{\rm vir}$ of 1.8 Mpc. The cluster, selected from a 300-Mpc cube simulation (Diemand, Moore & Stadel 2004b) with cosmological parameters $\Omega_\Lambda = 0.732$, $\Omega_m = 0.268$ and $\sigma_8 = 0.9$ (Spergel et al. 2003), was resimulated at high resolution and corresponds to the intermediate resolution cluster D9 of Diemand, Moore & Stadel (2004a). The number of particles within the virial radius is ∼6 × 10^6 and the softening length is 2.4 kpc.

At $z = 0.5$, we replaced 20 random cluster particles (10 within the virial radius and 10 within 20 per cent of the virial radius) with the high-resolution galaxy model. Only one galaxy model is used, in order to isolate the effects of orbit on the evolution. We assigned to the centre of mass of each galaxy the same orbital position and velocity

of the replaced particle. We replace particles rather than haloes so as not to bias the results by omitting 'overmerged' haloes. Internal velocities and lengths were rescaled according to the redshift and cosmology. In particular, the comoving velocities at a given redshift z are expressed in terms of the Hubble constant $H(z)$ through the relation

$$v = \frac{\dot{r}}{a} - H(z)\,x, \tag{4}$$

where r and x are the physical and comoving coordinates, respectively, and a is the scalefactor $1/(1+z)$.

3 GALAXY EVOLUTION

Among the initial sample of 20 galaxies, only 13 are still within the cluster virial radius at $z = 0$, while the others lie on bound orbits between $R_{\rm vir}$ and $1.5R_{\rm vir}$. This result is consistent with the fact that about half of the haloes which are presently at the outskirts of the cluster (up to $2R_{\rm vir}$) have a pericentre smaller than $R_{\rm vir}$ (Moore, Diemand & Stadel 2004).

The evolution of many of the galaxies within the cluster is quite violent, which is due to a sequence of strong gravitational encounters with substructures and the global cluster potential. Most of the central galaxies lose a significant fraction of stars and undergo a complete morphological transformation from discs to spheroidal systems. In order to highlight the presence of hidden structures, we applied to the stellar component of the simulation results the unsharp masking technique (Buta & Crocker 1993; Erwin & Sparke 2002) as described in Barazza et al. 2002. This method consists of the following steps. The intensity of each pixel is replaced with the mean intensity of a given area around the pixel producing a smoothed image. The linear dimension of this area has to be close to the typical scale of the features that we want to uncover. The original image is then divided by the smoothed one. Fig. 3 illustrates the results of the unsharp masking applied to a galaxy of our sample, where the ESO's MIDAS task FILTER/SMOOTH is used for the image smoothing with a smoothing length of 30–40 pixel, corresponding to ∼2 kpc.

Fig. 4 represents the different phases of the evolution of a galaxy transforming into a dE. The first stage of the evolution is characterized by the formation of a strong bar (Moore et al. 1998) and an open spiral pattern in the disc. The spiral arms are easily stripped, while the remaining material forms a ring structure around the bar. The bar+ring phase is quite stable and is apparent in the final state of several of the remnant galaxies. Often the ring is not directly visible in the simulation output, but is clearly seen after applying the unsharp masking. When gravitational heating due to tidal interactions removes the remaining spiral and ring features, only a naked bar remains. The bar usually undergoes a strong buckling instability and as a result the central part of the galaxy becomes more spherical. The buckled bar is subjected to further tidal heating and loses mass from its edges, becoming rounder the more encounters it suffers and the longer it evolves near to the cluster centre. Fig. 5 illustrates the evolution of bar and buckling instabilities for a representative galaxy which is orbiting close to the centre of the cluster at $z = 0$. $A_{\rm bar}$ and $A_{\rm buckling}$ are the bar and buckling amplitudes, defined, respectively, as the Fourier decomposition of the phase of particles in the xy plane and of their vertical positions (Sparke & Sellwood 1987)

$$A_{\rm bar} = \frac{1}{N}\left|\sum_j \mathrm{e}^{2i\phi_j}\right| \tag{5}$$

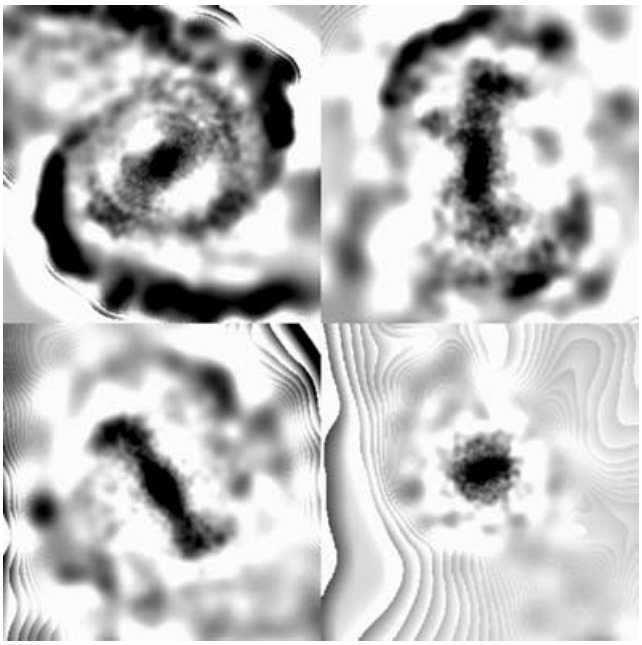

Figure 4. Morphological transformation (face-on projection) of a disc galaxy into a dwarf elliptical (GAL8 of Table 1). From the top left to the bottom right: at $t = 0.5$ Gyr from the beginning of the simulation, and $t = 1.4$, 2.4, 4.8 Gyr. The box size is ∼20 kpc. The step-like structures visible at the edges of the galaxies are due to features present in the low-density regions of the original smoothed stellar surface density maps, which are amplified by the unsharp masking.

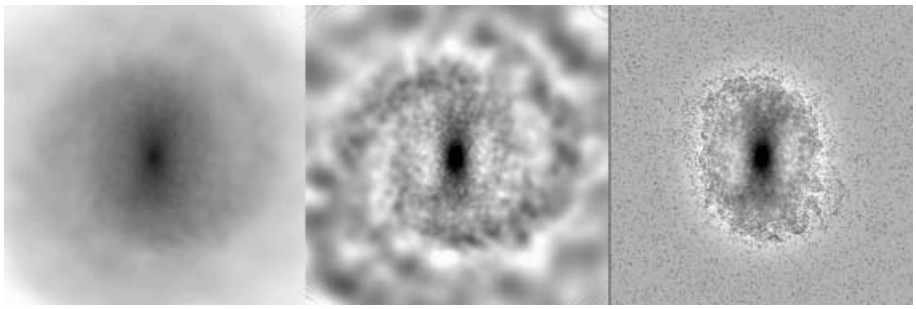

Figure 3. Unsharp masking technique applied to the stellar component of a simulated face-on galaxy (GAL5 of Table 1). The box size is ∼20 kpc. Left frame: smoothed stellar surface density produced from the simulation output using BEAM by J. Stadel. Middle frame: the result of the unsharp masking on the former image, which reveals presence of a bar and a spiral pattern. Right frame: a noise filter is previously applied to the original surface density map, increasing the intensity of the grey channel for randomly selected pixels. As a result in the final unsharp image, the low-density structures disappear and only the bar and a ring feature are still visible.

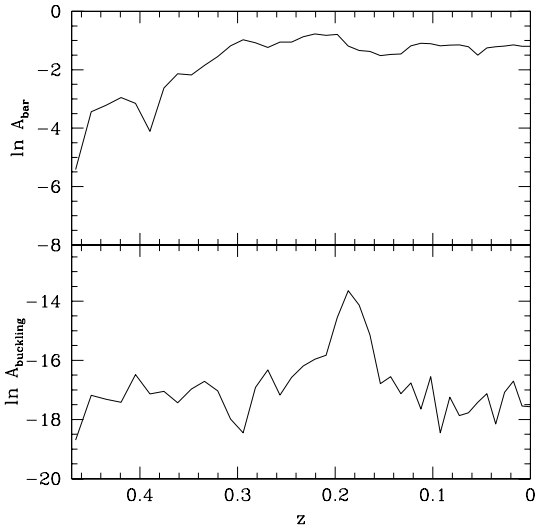

Figure 5. Evolution of a representative galaxy (GAL7 of Table 1). Top panel: strength of the bar. Bottom panel: buckling amplitude. The bar forms at $t = 1.1$ Gyr and strongly buckles at $t = 2.4$ Gyr.

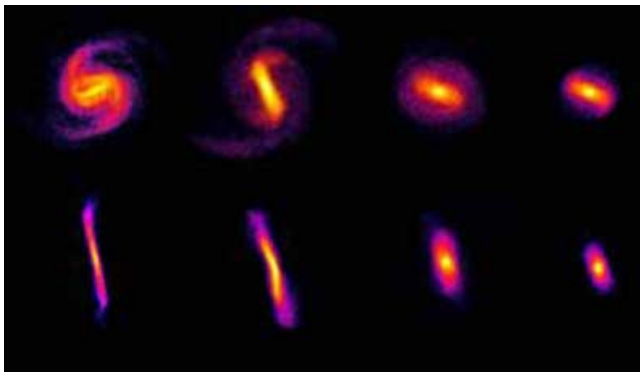

Figure 6. Evolution of the stellar surface density of GAL7 from $t = 1.4$ to 0 Gyr. The colour scale is logarithmic. The top panels represent the face-on projection, while the corresponding edge-on projection is shown on the bottom. The buckling phase, which has a peak at $t = 2.4$ Gyr, does not destroy the bar, but makes the central vertical structure of the galaxy thicker.

and

$$A_{\rm buckling} = \frac{1}{N}\left|\sum_j z_j {\rm e}^{2{\rm i}\phi_j}\right|. \quad (6)$$

Fig. 6 shows a face and edge-on projection of the same galaxy during the buckling phase where the bar appeared at $z = 0.3$.

Depending on the orbit and on the number of close encounters that the galaxy suffers, the morphological transformation of the stellar component can be complete and produce a pure spheroidal system, or can lead to the formation of a more elongated structure, which still retains disc and bar features (Fig. 7). For a few galaxies orbiting closest to the cluster centre, the tidal effects from the cluster potential become dominant and the evolution is very rapid. Fig. 8 shows the tidal tails generated by a strong impulsive encounter. The stripped mass is a significative fraction of the total stellar mass and the surface density in the tails is comparable with that of the outer disc. We do not expect that these kind of structures will be easily observable in clusters, since their lifetime is quit short (≈0.2 Gyr) due to numerous encounters with other substructures that heat and dissipate the stripped material. Stripped stars tend to create a diffuse distribution around the remnants (see Fig. 9), and in regions close to the centre it is almost impossible to distinguish well-defined stellar streams, even from the debris of a small fraction of the true number of dwarf galaxies in clusters.

Table 1 summarizes the main properties of the remnant galaxies. The initial model has a virial radius of 85 kpc and the effective radius of the stellar distribution is 2.5 kpc, defined as the radius containing half of the light of the galaxy. While almost all the galaxies lose more than two-thirds of the dark matter halo, galaxies located at outskirts of the cluster do not experience a significative amount of star loss, even if their stellar structure can be perturbed producing open spiral patterns and asymmetric features (last frame on the right of Fig. 7). For these remnants, the reduction of the effective three-dimensional radius, $r_{\rm e}$, is related to the formation of a bar that increases the central stellar density. On the other hand, galaxies orbiting closer to the cluster centre lose up to 90 per cent of their stellar mass, and the decrease of $r_{\rm e}$ corresponds to a real decrease in the size of the stellar component. In a few cases, the galaxy loses much more dark matter than stars and becomes baryon dominated in the central region. This is due to the fact that the orbits of the dark matter particles in the halo are more eccentric than those of the star particles, and therefore reach the tidal radius more easily. Table 1 shows that the loss of stellar mass is not a simple function of the mean orbital radius or apocentric/pericentric distance from the cluster centre, confirming the importance of harassment. According to Knebe et al. (2005), tidal interactions with other satellites account for about 30 per cent of the total mass loss experienced by a satellite halo. The last two columns of Table 1 give the mean axial ratios within $2r_{\rm e}$. There is a clear correlation between the *c*/*a* ratio (the flattening of the stellar component) and the final stellar mass. As shown in Fig. 10, massive stellar remnants have smaller *c*/*a* values and retain more of their initial disc nature, while galaxies that have lost most of their stars tend to be more spheroidal. The final state is always quite prolate, with the exception of GAL6 and GAL8 (the first two points in the upper left corner of Fig. 10), which are close to spherical. In the case of the less perturbed galaxies, this is due to the fact that the radius $2r_{\rm e}$ defines an area roughly corresponding to the bar region, while most of the other galaxies retain part of the radial anisotropy that originated during the bar phase (Mayer et al. 2001). Fig. 11 illustrates the morphological and kinematic evolution of the stellar component of four representative galaxies of our sample. Each set of three panels represents the galaxy distance from the central cluster (top), the axial ratios (middle) and the ratio between the maximum rotational velocity $v_{\rm max}$ and the mean velocity dispersion $\bar{\sigma}$ (bottom) as a function of time. All these quantities are measured within $2r_{\rm e}$. Both shapes and kinematics are not characterized by a smooth evolution, but present peaks and drops not necessarily connected to pericentric passages and indicative of tidal effects associated with close encounters with substructures. The initial steep decrease in the *b*/*a* ratio is instead related to the formation of the bar in the inner regions of the disc.

4 PHOTOMETRIC ANALYSIS

In order to compare the results of our simulations with observations, and in particular with Barazza, Binggeli & Jerjen (2003), we selected the remnants within the virial radius at $z = 0$ (first 13 galaxies of Table 1) and projected them along a random line of sight.

The isodensity contours of the projected discs were fitted with ellipses using the MIDAS task FIT/ELL3. The ellipses' centres, ellipticity and position angle were considered as free parameters

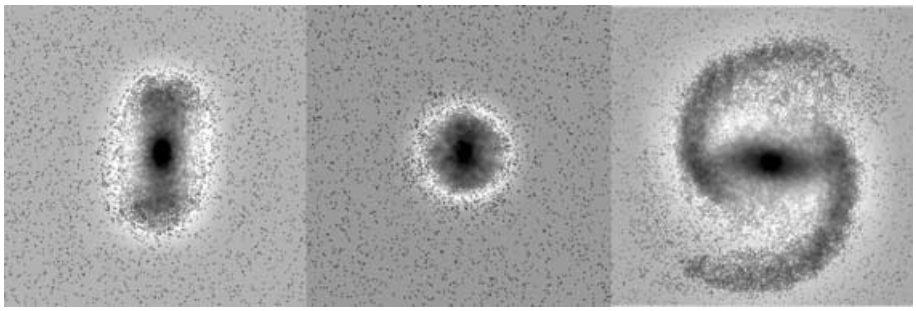

Figure 7. Three different final states of the harassed galaxies (unsharp nosified images). From left to right: bar-like galaxy (GAL7 of Table 1), spherical spheroid (GAL6) and spiral galaxy (GAL3). The addition of noises often hides ring structures surrounding the central bar, which is the case of the first remnant on the left. In order to point out the characteristic structure of the remnants we used two physical scales: the two images on the left have a box side of ∼12 kpc, while the box size of the spiral galaxy on the right is ∼30 kpc.

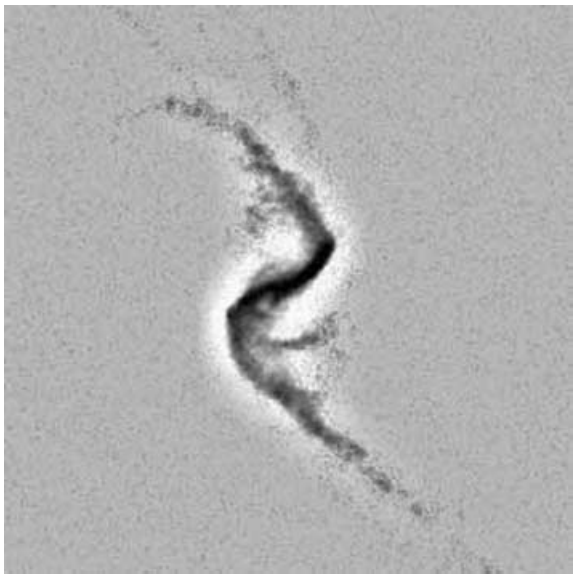

Figure 8. Tidal tails of GAL6 (Table 1) generated during a pericentric passage (unsharp noisified image). These smooth features are visible only for a short time (typically about 0.2–0.3 Gyr) since they are heated and evaporated by continued encounters with cluster substructures.

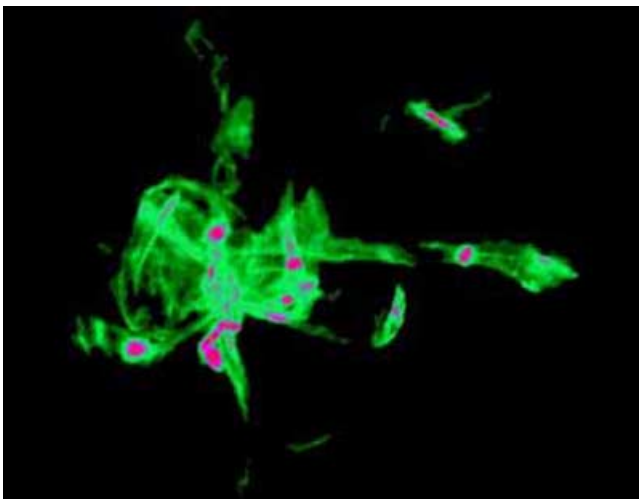

Figure 9. Intracluster light produced by tidal processes. The colour contrast is chosen in such a way as to point out the low-density regions (light green, corresponding to a surface brightness $\mu \lesssim 30$ mag arcsec^{-2}) and the traces of stellar streams.

of the fitting procedure. The isophotal contours of a representative galaxy (GAL9) are shown in Fig. 12. Ellipticity and position angle profiles are plotted in Fig. 13, where the independent variable is the equivalent radius $r_{\rm p} = \sqrt{a_{\rm p} b_{\rm p}}$, and $a_{\rm p}$ and $b_{\rm p}$ are the major and minor axis of the projected remnant. Even though there is no well-defined trend in the ellipticity profiles, galaxies that preserve a bar component are generally characterized by large ellipticities in the central 2–3 kpc and by a drop in the outer regions. Often, the inner 0.5 kpc exhibits a very low ellipticity corresponding to a small nuclear component produced by buckling instabilities, whereas the external drop is more likely due to disc heating. Rounder systems have a wider range of profiles, with eccentricities that may even increase with radius, as in the case of GAL1

The next step of this analysis consists of calculating the surface brightness profiles of the projected remnants. In order to derive a luminosity, we need to assign an M/L. We expect that the ISM would be rapidly stripped by ram pressure effects such that star formation is truncated shortly after the galaxies enter the cluster environment. In this case, roughly 8 Gyr from the beginning of the simulation, the stellar M/L will have increased by about a factor of 1.5–2 (Mayer et al. 2001). For this reason, we used a B-band $M/L \sim 6$ for the final remnants. The cumulative light profiles were determined by integrating the light of each galaxy in elliptical apertures with increasing equivalent radius (MIDAS task INTEGRATE/ELLIPS) and fixed centre, ellipticity and position angle. For these parameters, we adopted their mean values within a radius corresponding to half of the disc size, in order to avoid uncertainties in the isophote-fitting procedure due to the low-density external regions. In Table 2, we list the effective radius of each projected galaxy defined by $r_{\rm ep}$, which is the radius at which the cumulative light profile reaches half of the value that it has at the isophotal level of 28 mag arcsec^{-2} (upper B-band magnitude limit in Barazza et al. 2003).

The surface brightness profiles, obtained by differentiating the cumulative light curve with respect to the equivalent radius $r_{\rm p}$ (Barazza et al. 2003), are plotted in Fig. 13. The oscillation in the profiles of GAL3 and GAL12 reveals the presence of spiral arms viewed almost face on (Fig. 14), which enhance the local stellar density and produce abrupt changes in the position angle and eccentricity profiles.

The intensity profiles between 0.1 kpc (softening length for the stellar component) and the isophotal level of 27 mag arcsec^{-2} were

Table 1. Final state of the remnants. The second column indicates, when available, the apocentric and pericentric distances of the last orbit. For each galaxy, we list three-dimensional (spherically averaged) tidal r_t and effective r_e radius (in kpc), dark matter M_h and stellar M_s mass (in units of 10^9 $M_\odot$). The tidal radius is calculated using SKID (Stadel 2001), while r_e is the radius containing half of the light. The last two columns indicate the axial ratios (intermediate and short axis to major axis, respectively) measured within $2r_e$.

Galaxy	Apo-peri	r_t	r_e	M_h	M_s	*b*/*a*	*c*/*a*
GAL1	200-90	8.5	2.0	2.6	2.3	0.79	0.40
GAL2	150-100	10.1	1.3	2.8	2.4	0.58	0.39
GAL3	650-60	16.6	2.7	13.0	4.2	0.98	0.18
GAL4	300-50	11.6	1.8	5.2	3.2	0.44	0.34
GAL5	630-100	19.4	1.9	7.6	3.3	0.62	0.27
GAL6	90-40	3.6	0.7	0.2	0.5	0.90	0.79
GAL7	75-210	11.0	1.8	4.2	3.3	0.55	0.31
GAL8	100-60	4.6	1.1	1.0	1.5	0.87	0.86
GAL9	120-70	7.9	1.1	1.5	1.8	0.66	0.54
GAL10	270-80	9.0	1.2	1.8	1.8	0.62	0.49
GAL11	1130-120	16.9	2.6	14.6	4.1	0.66	0.18
GAL12	720-210	14.7	2.6	18.8	4.1	0.45	0.23
GAL13	1720-450	16.8	2.9	21.6	4.2	0.34	0.22
GAL14	...-460	17.2	2.0	8.2	3.6	0.71	0.18
GAL15	...-900	17.4	2.6	19.2	4.2	0.41	0.28
GAL16	...-...	16.3	2.5	24.4	4.2	0.79	0.29
GAL17	2480-...	17.0	2.9	21.1	4.2	0.43	0.19
GAL18	...-...	15.6	2.6	21.0	4.2	0.38	0.22
GAL19	2290-...	15.2	2.7	19.5	4.2	0.41	0.25
GAL20	2810-...	15.0	3.0	19.6	4.2	0.77	0.17

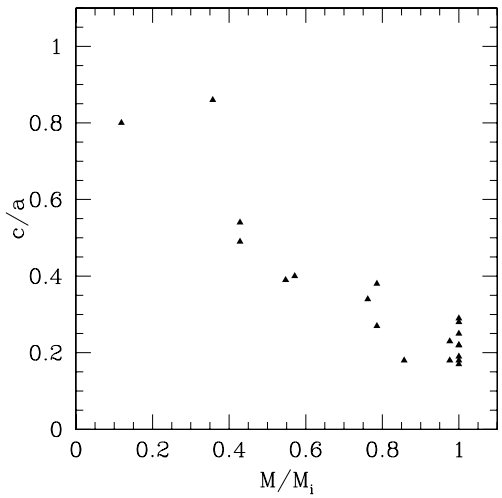

Figure 10. Final flattening of the remnants plotted versus the fraction of stellar mass within the tidal radius at $z = 0$.

fitted with a Sérsic profile

$$I(r) = I_0 e^{(-r/r_0)^{1/n}}, \quad (7)$$

where I_0 (central intensity), r_0 (scalelength) and n (shape parameter) are the free parameters of the fit. For $n = 1$ the Sérsic model corresponds to an exponential law, while a shape parameter $n = 4$ is indicative of a de Vaucouleurs profile. Converting intensities to surface brightnesses, equation (7) becomes

$$\mu(r) = \mu_0 + 1.086(r/r_0)^{1/n}, \quad (8)$$

where μ_0 is the surface brightness corresponding to I_0.

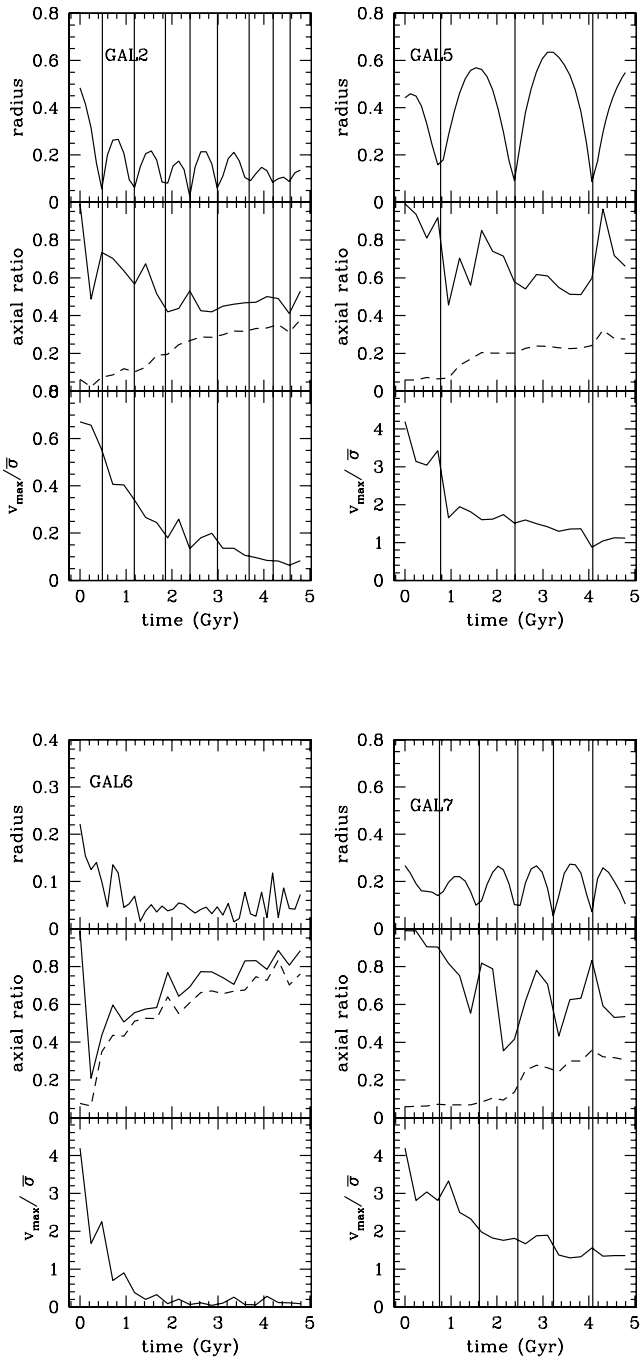

Figure 11. Each set of three vertical panels represents the morphological and kinematic evolution of a galaxy from Table 1: orbital radius (top panel), axial ratio (centre) and anisotropy parameter (bottom). In the middle panel, the solid line represents the intermediate/major axis ratio *b*/*a*, while the dashed line is the short/major axis ratio *c*/*a*. The vertical solid lines indicate the pericentric passages. Note that the vertical scale of the top panel in GAL6 differs from the others.

The fitting curves and parameters of those galaxies for which it was possible to fit with a Sérsic model are indicated in Fig. 13. The range of surface brightness parameters agrees quite well with the observations of dwarf galaxies in Virgo. The central surface brightness of our remnants is on average slightly higher than the values observed in *B*-band by Barazza et al. 2003, who fitted Sérsic profiles over similar radial intervals, the scalelengths obtained from the

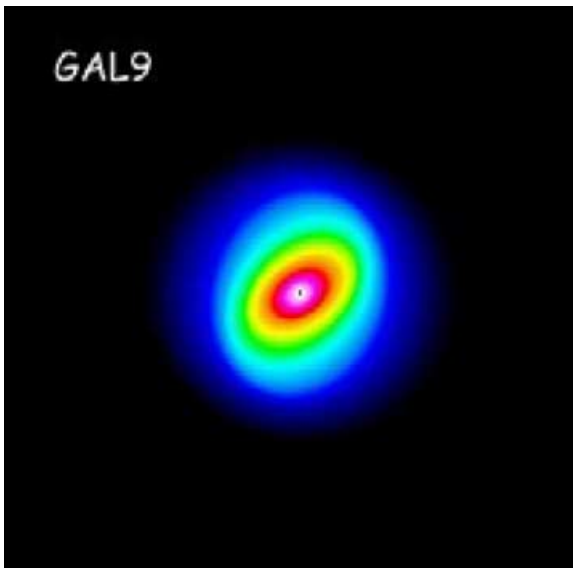

Figure 12. Elliptical contours of GAL9. A strong isophotal twist is evident in the outer region (see also Fig. 13).

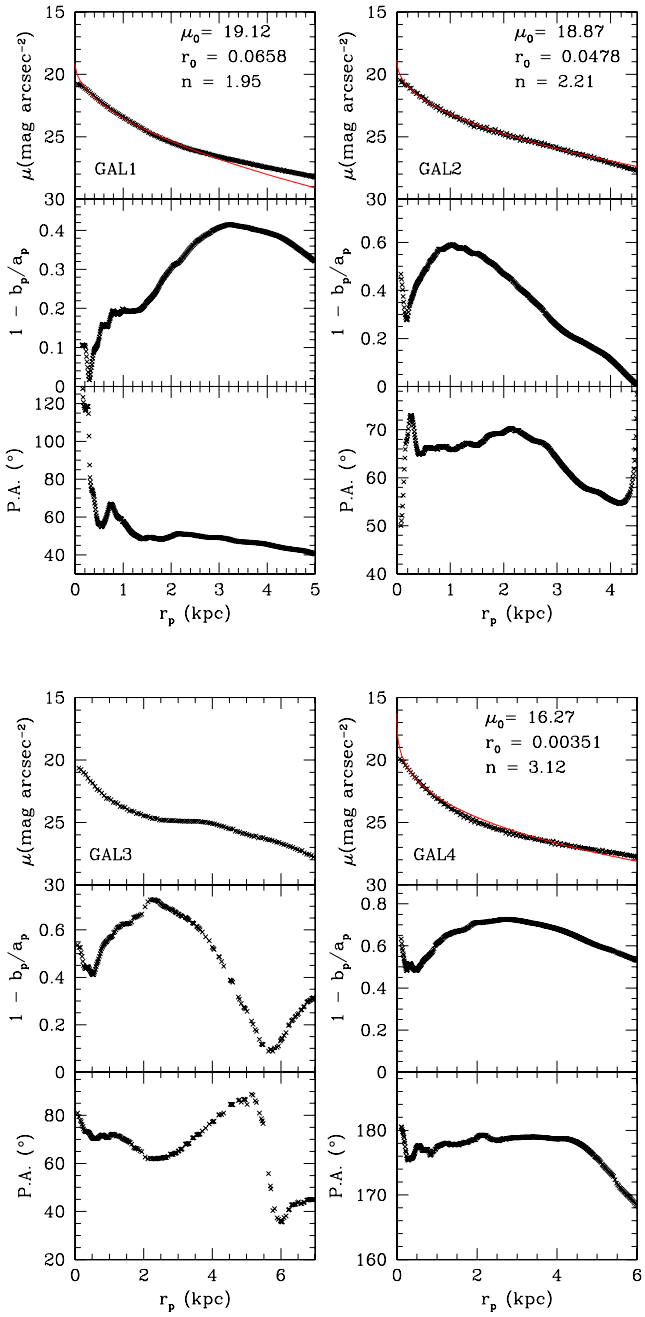

Figure 13. Each set of three vertical panels represents the photometric characteristics of a galaxy from Table 1: *B*-band surface brightness (top panel), ellipticity (centre) and position angle profile (bottom). The coordinate $r_{\rm p}$ is the equivalent radius $r_{\rm p} = \sqrt{a_{\rm p} b_{\rm p}}$, where $a_{\rm p}$ and $b_{\rm p}$ are the major and minor axes of the projected remnant. The Sérsic $r^{1/n}$ model is superimposed on the surface brightness profile (red solid line) and the corresponding best-fitting parameters are given in the top right of the panel. The central surface brightness μ_0 is expressed in 'mag arcsec^{-2}', r_0 is in 'kpc' and the shape parameter n is a pure number, which represents the deviation of the profile from an exponential law.

fitting procedure are comparable with their results. Also note that the quoted central surface brightness values are Sércic fits extrapolated to $r = 0$. The actual values at our resolution limit are somewhat fainter (Table 3). Galaxies with the smallest values of the shape parameter, n, are not well fitted by a Sérsic profile in the central part. This is the case of GAL4 – apparently a pure spheroidal system with high ellipticity, in reality characterized by a disc component seen edge-on – and of GAL7, which is still an asymmetric bar-like system with a large central nuclear component with small ellipticity values. For GAL7, we also show surface brightness profiles, ellipticity and position angles for the face-on and the end-on projections (Fig. 15). The smallest central ellipticity is associated with the end-on projection, where the bar is viewed down the major axis. Only the less massive remnants GAL6 and GAL8 have surface brightness profiles approaching to exponentials ($n \sim 1$).

5 KINEMATICS

We attempt to measure the kinematics of the remnants in a similar way as previous authors measuring dwarf galaxies in the Virgo cluster. We measure the kinematics of the 13 projected galaxies analysed in Section 4 using a 0.3×12 kpc slit, which corresponds, at the distance of Virgo (15.3 Mpc, Freedman et al. 2001) to 3×40 arcsec^2. This radial range is comparable with the slit length adopted by van Zee et al. 2004a and allows us to observe in most of the galaxies the turnover of the rotation curve, while the thickness of the slit was set to the softening length of 0.1 kpc. The slit was positioned along the major axis of the projected remnant centred on the galaxy, and star particles within the slit area were binned into a grid. For each grid interval with more than 15 particles – excluding thus the most weakly bound particles at the edges of the system – we calculated the mean particle velocity (relative to the centre of mass of the galaxy) and velocity dispersion along the line of sight. For the two smallest remnants GAL6 and GAL8, we increased the number of bins in order to obtain more precise velocity curves. The resulting kinematic profiles are indicated in Fig. 16, where for each galaxy the line-of-sight velocity (left-hand panels) and velocity dispersion (right-hand panels) are plotted as a function of the radial distance along the major axis. In most of the cases, the remnants lose a large fraction of rotation velocity, but only for one galaxy (GAL6) we do not observe any significative rotation along the major axis. GAL8 shows a well-defined symmetric rotation pattern although its peak velocities is only $\sim$7 km s^{-1}. GAL6 and GAL8 do not show

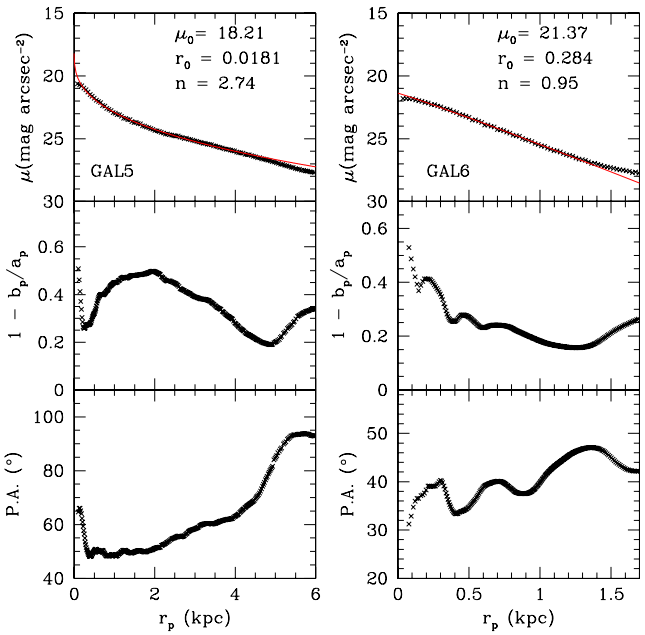

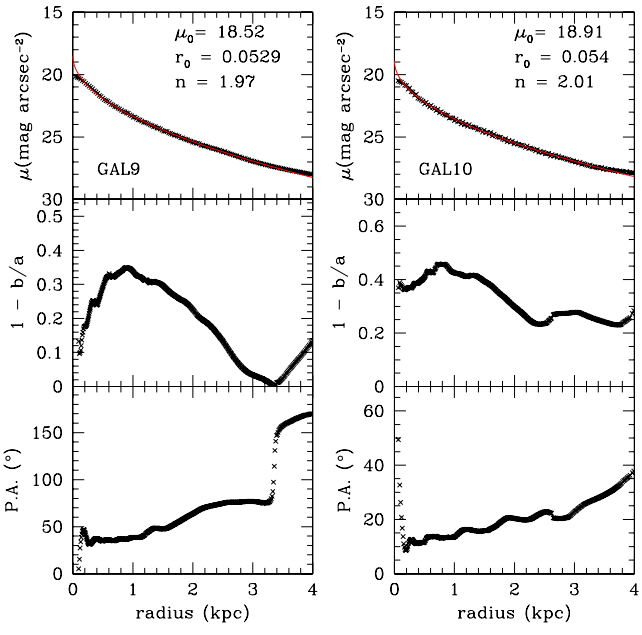

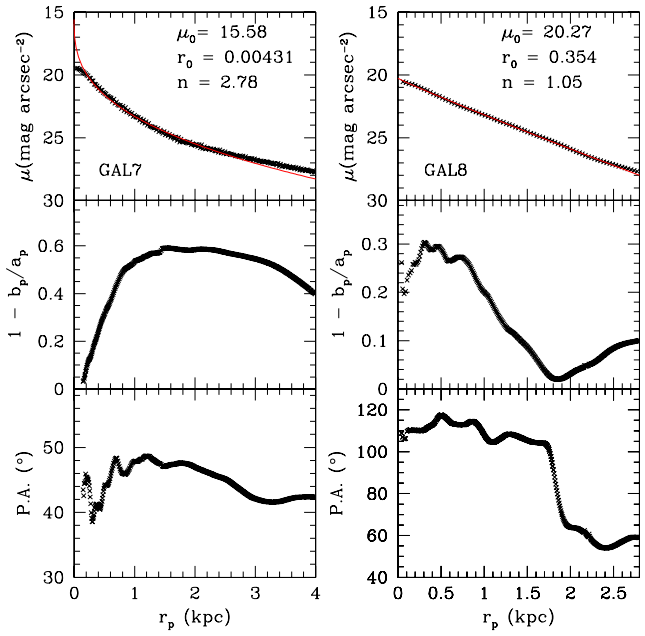

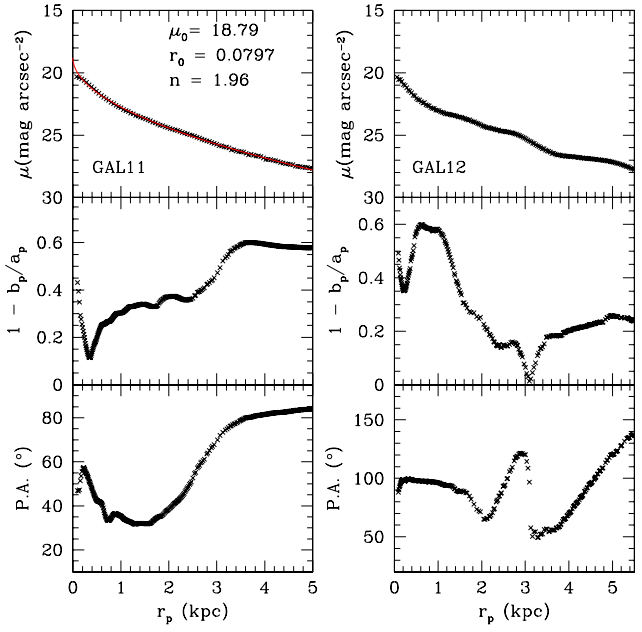

Figure 13 – *continued*

Figure 13 – *continued*

evidences for structures or disc features and are spheroidal systems with a *c*/*a* ratio larger (Table 1) than the other remnants and surface brightness profiles well fitted by exponential laws. Moreover, they are quite small ($M_s \leqslant 1.5 \times 10^9$ $M_\odot$) baryon-dominated galaxies presently orbiting at ≈100 kpc from the cluster centre.

Is the lack of rotation observed in GAL6 due to a projection effect, i.e. we are looking at the face-on projection of a rotating system, or is it physically significative? Fig. 17 illustrates the kinematic profiles of GAL6 and GAL8 for different inclinations of the remnant: from the top to the bottom $i = 0°$, which corresponds to a face-on projection, $i = 45°$ and $90°$ (edge-on). The last panel on the bottom represents an end-on galaxy, with inclination $i = 90°$ and the three-dimensional major axis aligned with the line of sight. GAL6 shows traces of rotation only for $i = 0$, with a maximum rotational velocity $v_{max} = 3.7$ km s^{-1}, while the other projections have no well-defined rotation curves and values of $v_{max} \lesssim 2.7$ km s^{-1}. In the case of non-rotating galaxies, we estimated an upper limit for v_{max} by differentiating the average velocities on each side of the major axis and dividing by 2 (Geha et al. 2002). In the calculation of v_{max} for $i = 0°$ and $90°$ we excluded points with velocity dispersion larger than 80 km s^{-1}, representing stars close to the tidal radius of the remnant. The projected motion of these stars with respect to the centre of mass is due to stripping processes and not rotation. On the other hand, GAL8 has always a well-defined rotation pattern

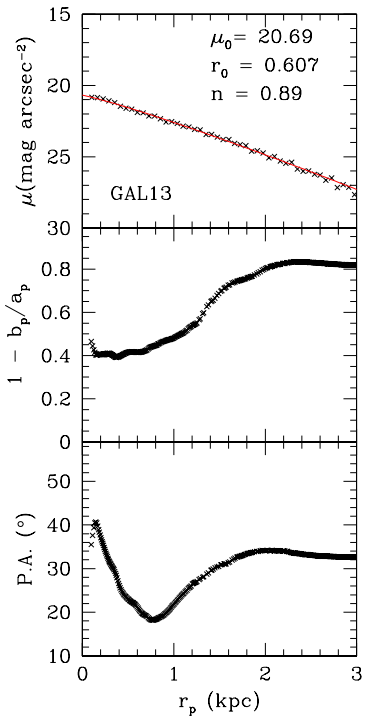

Figure 13 – *continued*

Table 2. Effective radii (in kpc) of the projected remnants calculated using the integrated light curves. In most of the cases, they do not deviate considerably from the values obtained for the three-dimensional galaxies. A significative exception is GAL13, a disc system viewed almost edge-on.

Remnant	r_{ep}	Remnant	r_{ep}
GAL1	1.9	GAL8	1.0
GAL2	1.7	GAL9	1.4
GAL3	2.7	GAL10	1.5
GAL4	2.4	GAL11	1.9
GAL5	2.3	GAL12	2.0
GAL6	0.6	GAL13	1.1
GAL7	1.5		

and there is no preferential direction with zero rotation. Among the other galaxies characterized by low rotation velocities (see Fig. 16), GAL2, GAL9 and GAL10 are more massive systems compared to the two spheroids GAL6 and GAL8, but have still high *c/a* values, while the low line-of-sight velocity of GAL12 is not related to a morphological transformation, but is simply due to the fact that it is a spiral galaxy viewed face on (Fig. 14).

On the basis of this limited sample we expect non-rotating and slowly rotating dwarfs to have internal and environmental properties substantially different from the rotating ones. In particular, the former seems to be the product of a violent morphological transformation accelerated by the proximity of the cluster centre. This result is apparently in contradiction with Geha et al. (2003), who finds no relationship between the amount of rotation and the morphology or the orbital properties of the galaxies in their sample.

From Fig. 16 it appears evident that although the galaxies lose significant amounts of mass, the velocity dispersion can rise up to 50 km s^{-1} in the central 1–2 kpc. This is due to the bar formation

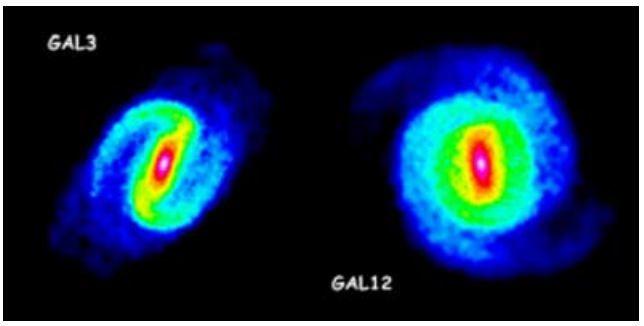

Figure 14. Surface density distribution of the two remnants presenting a nearly face-on spiral pattern. The physical size of both the images is ∼12 kpc.

Table 3. Parameters of the Sérsic fit: central surface brightness (in mag arcsec^{-2}), surface brightness at the softening radius, scalelength (kpc) and shape parameter.

Galaxy	μ_0	μ (0.1 kpc)	r_0	n
GAL1	19.12	20.50	0.0658	1.953
GAL2	18.87	20.38	0.0478	2.208
GAL4	16.27	19.44	0.00351	3.115
GAL5	18.21	20.24	0.0181	2.740
GAl6	21.37	21.79	0.284	0.949
GAL7	15.58	18.95	0.00431	2.778
GAL8	20.27	20.60	0.354	1.054
GAL9	18.52	20.02	0.0529	1.972
GAL10	18.91	20.39	0.054	2.008
GAL11	18.79	20.01	0.0797	1.957
GAL13	20.69	20.83	0.607	0.885

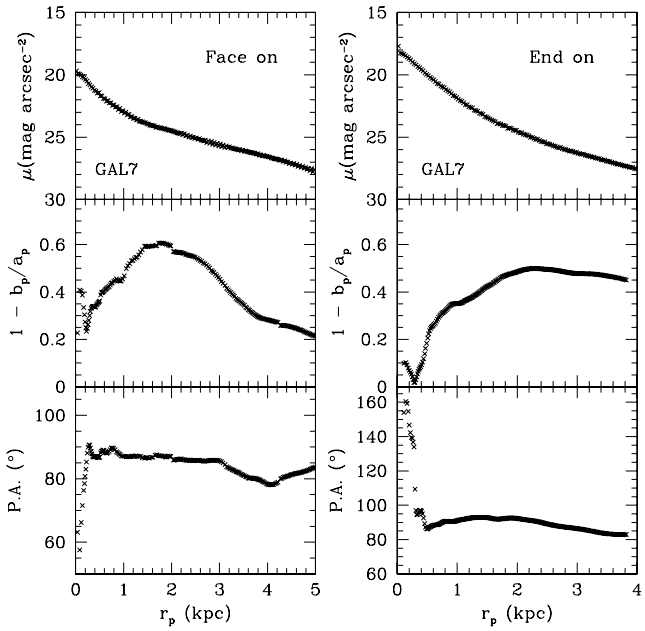

Figure 15. *B*-band surface brightness, ellipticity and position angle profiles of the face-on and end-on projections of GAL7.

and the transformation of circular to more radial orbits. The velocity dispersion profiles are typically decreasing at larger radii, but they rise again in those galaxies for which the slit semilength approaches or exceeds the tidal radius.

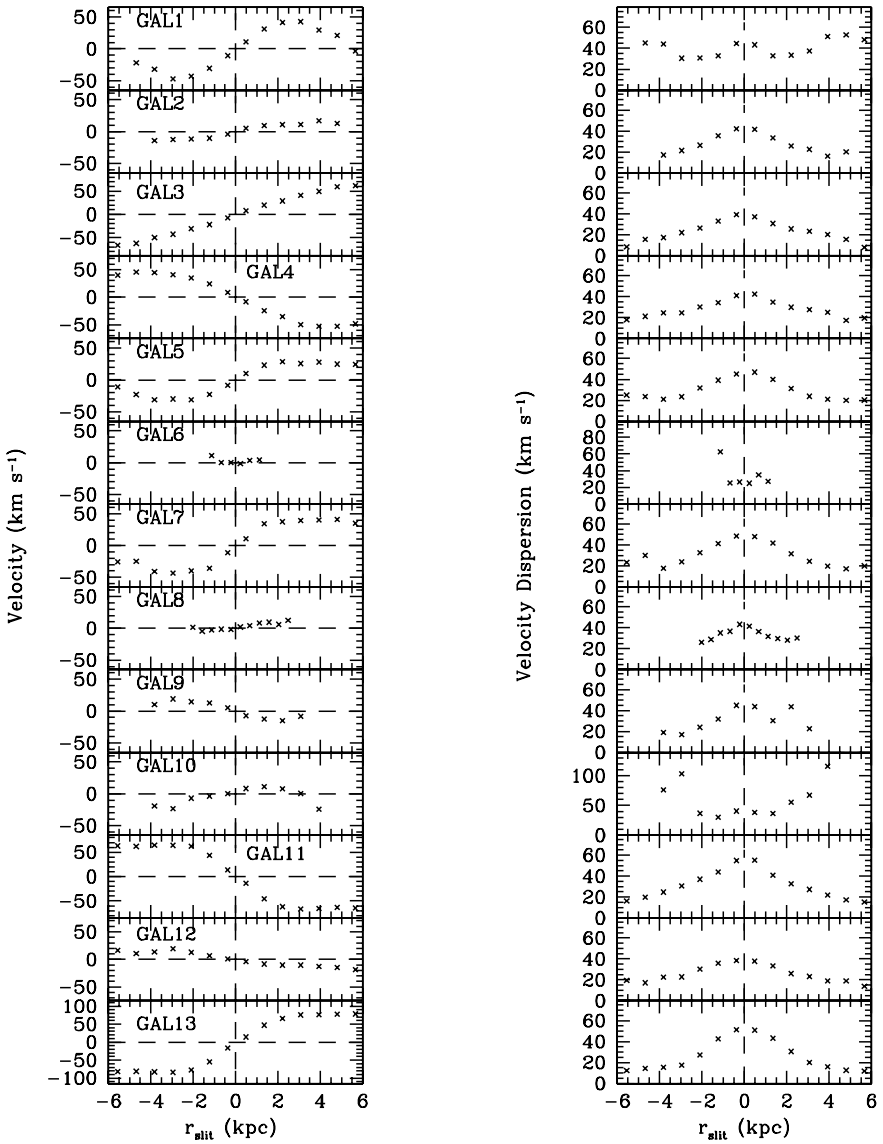

Figure 16. Projected kinematic profiles of the remnants within the cluster virial radius at $z = 0$. The line-of-sight velocity (left-hand panels) and the velocity dispersion (right-hand panels) are plotted as a function of the radial distance along the major axis.

As the ratio between rotational velocity and velocity dispersion decreases, the galaxy loses rotational support and the flattening becomes dominated by anisotropic pressure. The degree of rotational support can be expressed in terms of the anisotropy parameter $(v/\sigma)^*$ (Binney 1978), defined as

$$(v/\sigma)^* = \frac{v/\bar{\sigma}}{\sqrt{\epsilon(1-\epsilon)}}, \tag{9}$$

where v is the rotational velocity, $\bar{\sigma}$ and are ϵ the mean projected velocity dispersion and ellipticity, respectively. The theoretical prediction for a rotationally flattened spheroidal is given by $(v/\sigma)^* \sim 1$ (Binney & Tremaine 1987) and is represented in Fig. 18 by a continuous solid line. Galaxies well below this curve have significant velocity anisotropy.

In order to compare our results with observations, we plotted in Fig. 18 the ratio of the maximum rotational velocity, $v_{\rm max}$, to the mean velocity dispersion, $\bar{\sigma}$, within a radius of 6 kpc versus the mean isophotal ellipticity calculated in the same radial range. In the same plot, we show the observational results for most of the dwarf galaxies in Virgo with published kinematics. We also plot the data for dwarf galaxies in the Fornax cluster by De Rijcke et al. (2003). Some of the galaxies in Fig. 18 (VCC 543, VCC 917, VCC 1036, VCC 1261 and VCC 1308) were observed by both Geha et al. (2003) and van Zee et al. (2004a), using the Keck II and Palomar telescope. The observations of van Zee et al. (2003), which cover a larger radial extent due to the aperture size, gives to significantly higher values of $v_{\rm max}$ with respect to Geha et al. 2003. This appears to be due to the fact that the smaller slit used by the latter authors only samples the inner rising part of the rotation curve and does not include the maximum value. For example, VCC 917 and VCC 1308, classified as non-rotating galaxies (both with $v_{\rm max} = 0.4$ km s^{-1}) by Geha et al. 2003, have $v_{\rm max} > 10$ km s^{-1} according to van Zee et al. 2003, while the rotation curves of the slowly rotating dwarfs VCC 543 and VCC 1036 ($v_{\rm max} = 13$ and 14 km s^{-1} in Geha et al. 2003) peak beyond 15 arcsec with $v_{\rm max} >$ 40 km s^{-1}. Most of the simulated remnants have a similar range of

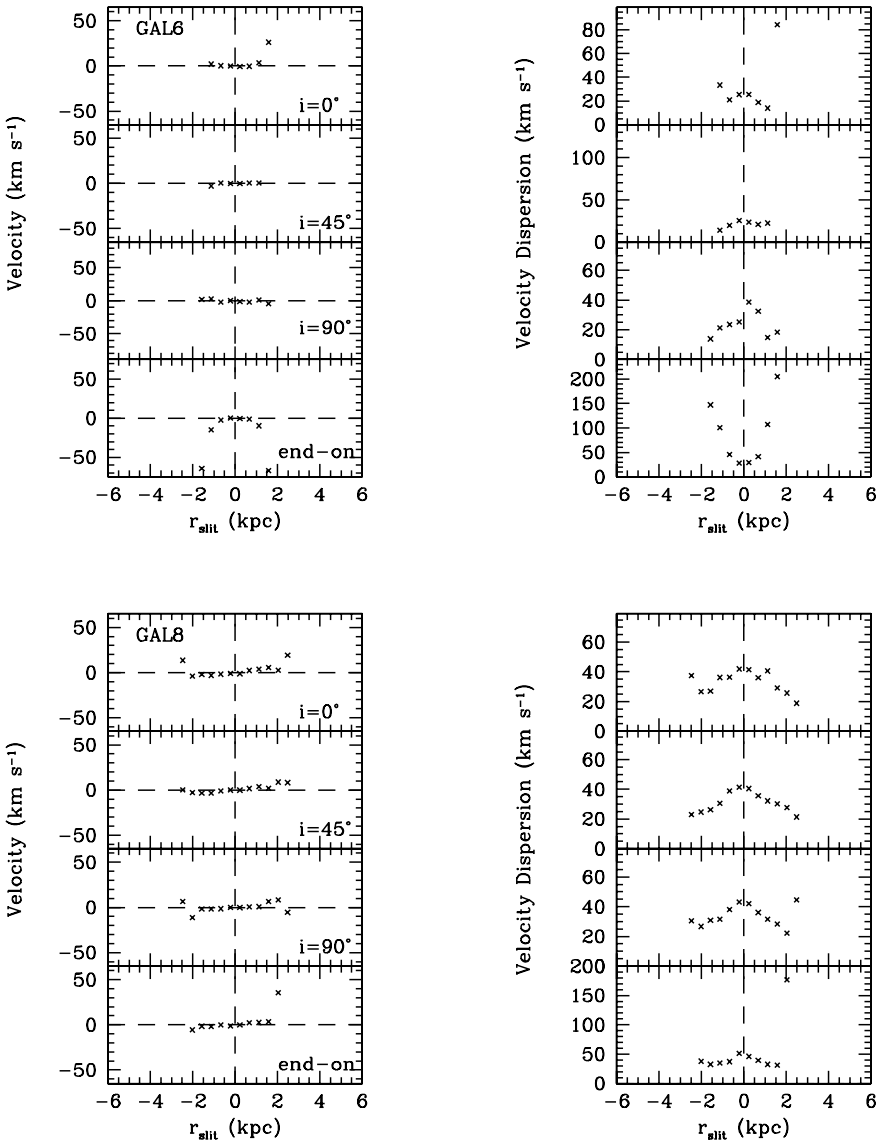

Figure 17. Projected kinematic profiles of GAL6 and GAL8 for $i = 0^\circ$ (face-on orientation), $i = 45^\circ$, $i = 90^\circ$ (edge-on) and $i = 90^\circ$ with the three-dimensional major axis aligned with the line of sight (end-on projection). The line-of-sight velocity (left-hand panels) and the velocity dispersion (right-hand panels) are plotted as a function of the radial distance along the projected major axis.

ellipticities and $v_{\rm max}/\bar{\sigma}$ as the observed dwarfs, even if it is clear that we have some difficulties in reproducing galaxies with a degree of rotational support close to zero. On the other hand, it is possible that the low $v_{\rm max}/\bar{\sigma}$ ratio of some galaxies is due to the small radial range covered by the observations. In order to understand how much the slit length influences the results, in Fig. 19 we plotted the v/σ ratio of the projected remnants as a function of the radial distance along the slit. In most of the cases, v/σ increases with radius (with the remarkable exception of GAL1 whose rotational support drops beyond $r = 2.5$ kpc). Using a 4-kpc slit, we would find 10 galaxies below $v_{\rm max}/\bar{\sigma} = 1$, three well below $v_{\rm max}/\bar{\sigma} = 0.1$, which is the upper limit assumed by Geha et al. (2003) for non-rotating dwarfs. Increasing the slit length up to 8 kpc, the number of galaxies with a low degree of rotational support is still quite high (seven galaxies with $v_{\rm max}/\bar{\sigma} < 1$ and four with $v_{\rm max}/\bar{\sigma} < 0.5$), but only GAL6 has still a $v_{\rm max}/\bar{\sigma} \sim 0$, as in the case of the adopted slit length of 12 kpc.

6 CONCLUSIONS

We follow the evolution of late-type disc galaxies as they evolve within a hierarchically forming galaxy cluster using N-body simulations. We use a single-galaxy model to explore the effects of cluster-centric position and orbit. Our resolution is such that we can compare with Keck and Palomar kinematics and Very Large Telescope (VLT) imaging data. We find the following.

(i) The cluster environment can be responsible for triggering bar and buckling instabilities.

(ii) Tidal shocks with dark matter substructures and the mean cluster potential are both important at driving the evolution from discs to spheroidal structures. However, galaxies within the inner 100 kpc suffer the most complete transformation and mass loss.

(iii) None of the discs are completely destroyed and since the surface brightness of our discs within two times the effective radius is well above the resolution limit of the *Hubble Space Telescope*

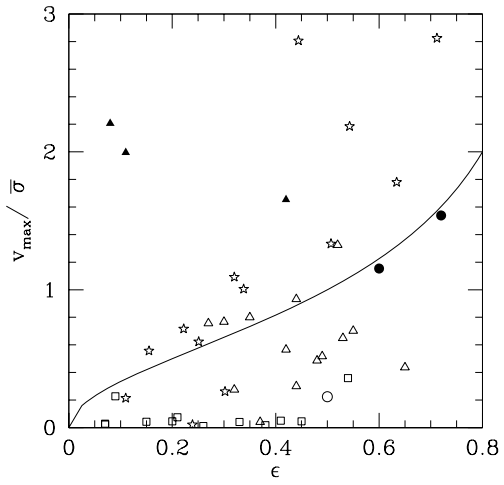

Figure 18. The ratio of the maximum rotational velocity, $v_{\rm max}$, to the mean velocity dispersion, $\bar{\sigma}$, plotted versus the mean isophotal ellipticity. Stars represent the simulated sample, while open triangles, open squares, filled triangles and open circles show observational data from van Zee et al. (2004a), Geha et al. (2003), Pedraz et al. (2002) and Bender & Nieto (1990), respectively. For galaxies observed both by Geha et al. (2003) and van Zee et al. (2004a) we assumed the values of $v_{\rm max}$ and $\bar{\sigma}$ provided by the latter work. Filled circles indicate data relative to dwarf spheroidals in the Fornax cluster from De Rijcke et al. (2003). The solid line represents the theoretical prediction for a galaxy flattened by rotation from Binney & Tremaine (1987).

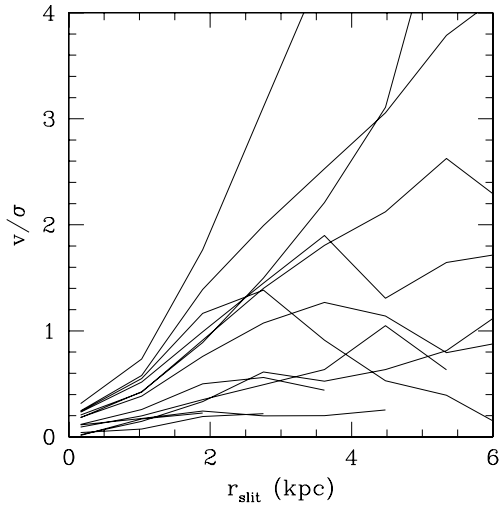

Figure 19. v/σ ratio as a function of the radial distance along the major axis for the 13 projected remnants of Fig. 16.

(*HST*) photometry (Drinkwater et al. 2003), we do not expect to create ultracompact dwarf (UCD) galaxies by progenitor discs with cuspy dark haloes.

(iv) More tidal heating leads to more mass loss, which leads to rounder galaxies.

(v) The kinematics (v/σ) of the stellar remnants is similar to observations of Virgo and Fornax dE/dSph galaxies. Only the most severely disrupted galaxies that lose most of their stellar mass become completely pressure supported. Most of the remnants retain a significant amount of rotational motion.

(vi) Unsharp masked images of the galaxies show similar hidden bar and spiral features as some cluster galaxies. These gradually disappear as the galaxies suffer more heating. Our results could be rescaled in time and mass to make statements about possible disc progenitors entering group or even galactic environments. The next step is to self-consistently follow the evolution of galaxies as they form and evolve in different environments.

ACKNOWLEDGMENTS

We would like to thank Jürg Diemand for providing the cosmological cluster simulation. We are grateful to Alister Graham, Andrea Macciò, Fabio Barazza, Marla Geha, Frank van den Bosch and Stelios Kazantzidis for useful discussions. The numerical simulations were performed on the Zbox (http:/www.theorie.physik.unizh.ch/stadel) supercomputer at the University of Zürich. CM and RP are supported by the Swiss National Science Foundation. VPD is supported by a Brooks Fellowship at the University of Washington.

REFERENCES

Barazza F. D., Binggeli B., Jerjen H., 2002, A&A, 391, 823
Barazza F. D., Binggeli B., Jerjen H., 2003, A&A, 407, 121
Bender R., Nieto J. L., 1990, A&A, 239, 97
Binney J., 1978, MNRAS, 183, 501
Binney J., Tremaine S., 1987, Galactic Dynamics. Princeton Univ. Press, Princeton
Buta R., Crocker D. A., 1993, AJ, 106, 939
Conselice C. J., Gallagher J. S., Wyse R. F. G., 2001, ApJ, 559, 791
Courteau S., 1997, AJ, 114, 2402
De Rijcke S., Dejonghe H., Zeilinger W. W., Hau G. K. T., 2001, ApJ, 559, L21
De Rijcke S., Dejonghe H., Zeilinger W. W., Hau G. K. T., 2003, A&A, 400, 119
Diemand J., Moore B., Stadel J., 2004a, MNRAS, 353, 624
Diemand J., Moore B., Stadel J., 2004b, MNRAS, 352, 535
Dressler A., Oemler A. J., Butcher H. R., Gunn J. E., 1994, ApJ, 430, 107
Drinkwater M. J., Gregg M. D., Hilker M., Bekki K., Couch W. J., Ferguson H. C., Jones J. B., Phillipps S., 2003, Nat, 423, 519
Erwin P., Sparke L. S., 2002, AJ, 124, 65
Ferguson H. C., Sandage A., 1991, AJ, 101, 765
Freedman W. L. et al., 2001, ApJ, 553, 47
Gavazzi G., Donati A., Cucciati O., Sabatini S., Boselli A., Davies J., Zibetti S., 2005, A&A, 430, 411
Geha M., Guhathakurta P., van der Marel R. P., 2002, AJ, 124, 3073
Geha M., Guhathakurta P., van der Marel R. P., 2003, AJ, 126, 1794
Gnedin O. Y., 2003, ApJ, 589, 752
Graham A. W., Guzmán R., 2003, AJ, 125, 2936
Hernquist L., 1993, ApJ, 86, 389
Jerjen H., Kalnajs A., Binggeli B., 2000, A&A, 358, 845
Knebe A., Power C., Gill S. P. D., Gibson B. K., 2005, MNRAS, submitted (astro-ph/0507380)
Kormendy J., Freeman K. C., 2004, Int. Astron. Union Symp., 220, 377
Mayer L., Governato F., Colpi M., Moore B., Quinn T., Wadsley J., Stadel J., Lake G., 2001, ApJ, 559, 754
Mayer L., Moore F., Quinn. T., Governato F., Stadel J., 2002, MNRAS, 336, 119
Mo H. J., Mao S., White S. D. M., 1998, MNRAS, 295, 319
Moore B., Katz N., Lake G., Dressler A., Oemler A., 1996, Nat, 379, 613
Moore B., Lake G., Katz N., 1998, ApJ, 495, 139
Moore B., Diemand J., Stadel J., 2004, in Diaferio A., ed., IAU Colloquium 195: Outskirts of Galaxy Clusters: Intense Life in the Suburbs. Cambridge Univ. Press, Cambridge, p. 513
Navarro J. F., Frenk C. S., White S. D. M., 1996, ApJ, 462, 563
Navarro J. F., Frenk C. S., White S. D. M., 1997, ApJ, 490, 493
Pedraz S., Gorgas J., Cardiel N., Sánchez-Blázquez P., Guzmán R., 2002, MNRAS, 332, L59

Persic M., Salucci P., 1997, in Persic M., Salucci P., eds, ASP Conf. Ser. Vol. 117, Dark and Visible Matter in Galaxies and Cosmological Implications. Astron. Soc. Pac., San Francisco, p. 148
Simien F., Prugniel P., 2002, A&A, 384, 371
Sparke L. S., Sellwood J. A., 1987, MNRAS, 225, 653
Spergel D. N. et al., 2003, ApJS, 148, 175
Springel V., White S. D. M., 1999, MNRAS, 307, 162
Stadel J., 2001, PhD thesis, Univ. Washington
Toomre A., 1964, ApJ, 139, 1217
Toomre A., 1981, in Fall S. M., Lynden-Bell D., eds., Structure and Evolution of Normal Galaxies. Cambridge Univ. Press, Cambridge, 111
van Zee L., Skillman E. D., Haynes M. P., 2004a, AJ, 128, 121
van Zee L., Barton E. J., Skillman E. D., 2004b, AJ, 128, 2797

This paper has been typeset from a TEX/LATEX file prepared by the author.